Materials Horizons

COMMUNICATION

View Article Online
View Journal

Cite this: DOI: 10.1039/c9mh00589g

Received 17th April 2019,
Accepted 10th June 2019

DOI: 10.1039/c9mh00589g

rsc.li/materials-horizons

Creating glasswing butterfly-inspired durable antifogging superomniphobic supertransmissive, superclear nanostructured glass through Bayesian learning and optimization†

Sajad Haghanifar,[a] Michael McCourt,[b] Bolong Cheng,[b] Jeffrey Wuenschell,[c] Paul Ohodnicki[c] and Paul W. Leu *[ade]

The creation of durable superomniphobic surfaces with optical functionality has been extremely challenging. Major challenges have included low optical transmission, low optical clarity, lack of scalable fabrication, condensation failure, and inability to self-heal. Inspired by recent research on the transmission advantages of the random nanostructures on the glasswing butterfly, we report on a strategy to create self-healing, random re-entrant nanostructured glass with high liquid repellency and antifogging properties with supertransmission (99.5% at 550 nm wavelength for double-sided glass) and superclarity (haze under 0.1%). Our approach to creating these random nanostructures is to utilize a multiobjective learning and Bayesian optimization approach to guide the experiments of glass substrate fabrication. The surface demonstrates static water and ethylene glycol contact angles of 162.1 ± 2.0° and 155.2 ± 2.2°, respectively. The glass exhibits resistance to condensation or anti-fogging properties with an antifogging efficiency more than 90% and demonstrates the departure of water droplets smaller than 2 μm. The surface can restore liquid-repellency after physical damage through heating for 15 minutes. We envision that these surfaces will be useful in a variety of optical applications where self-cleaning, antifouling, and antifogging functionalities are important.

New concepts

This paper demonstrates a design process that combines Bayesian learning and optimization with the physical intuition of the authors to create a new high-performance, multi-functional glass. The integration of machine learning methods and physical intuition enables us to efficiently search a high-dimensional fabrication space for creating random re-entrant nanostructures inspired by those on the glasswing butterfly. In particular, we pose a multiobjective optimization problem where we seek to balance the photon management and wettability properties of the surface, and determine a subset of the Pareto efficient frontier that is subject to pre-defined threshold values. We report on a self-healing supertransmissive and superclear nanostructured glass with high liquid repellency and antifogging properties. We envision that these surfaces will be useful in a variety of optical and optoelectronic applications where self-cleaning, anti-fouling, and anti-fogging are important.

Introduction

Natural surfaces such as lotus leaves, moth eyes, and butterfly wings have evolved over millions of years to optimize different surface functionalities related to survival and adaptation in different environments. Various unique micro- and nanostructures may be found in these natural surfaces that provide for functionalities such as antisoiling, self-cleaning, bacterial resistance, anti-fogging, and water harvesting.[1–6] Inspired by nature, researchers have sought to understand how different micro- and nanostructures provide for desired functionalities and utilized this knowledge to demonstrate a multitude of synthetic surfaces with novel functionalities.[7–11]

Many self-cleaning surfaces have been demonstrated[12–14] that are inspired by the superhydrophobic leaves of the *Nelumbo nucifera* (sacred lotus), which exhibit both high wetting contact angle (superhydrophobicity) and low contact angle hysteresis (adhesion) due to the combination of hierarchical surface morphology and hydrophobic epitcuticular wax.[15] Superhydrophobic surfaces may be created through low-surface energy micro-/nanostructures which promote Cassie–Baxter wetting,[16] where the water droplet contacts a small fraction of the surface due to air being trapped with the structures. This is in contrast to Wenzel wetting, where the water homogeneously contacts the surface.[17] Water droplets easily roll or bounce off superhydrophobic surfaces, while removing dust particles with them.

[a] Department of Industrial Engineering, University of Pittsburgh, Pittsburgh, PA 15261, USA. E-mail: pleu@pitt.edu
[b] SigOpt, San Francisco, USA
[c] National Energy Technology Laboratory, U.S. Department of Energy, Pittsburgh, PA 15236, USA
[d] Department of Mechanical Engineering, University of Pittsburgh, Pittsburgh, PA 15261, USA
[e] Department of Chemical Engineering, University of Pittsburgh, Pittsburgh, PA 15261, USA

† Electronic supplementary information (ESI) available. See DOI: 10.1039/c9mh00589g

While these surfaces effectively repel water, there is also great interest in surfaces that repel more types of liquids than just water. The ability to repel many liquids is referred to as superomniphobicity, where surfaces demonstrate a static contact angle greater than 150° and low contact angle hysteresis for a variety of liquids.[18–22] Creating surfaces that are superomniphobic is significantly more challenging than creating ones that are superhydrophobic. This is because the surface tensions of oil and other organic liquids are lower than water and thus, they tend to spontaneously spread across surfaces and past trapped air.[23–27] Springtail insects are the only known surface in nature that display apparent wetting contact angles $\theta > 150^\circ$ and low hysteresis for a wide range of fluids.[27] Recent research has suggested that the key to obtaining superomniphobicity is re-entrant structures or surfaces with concave topographic features, which provide for robust metastable trapped air interfaces.[22]

While many synthetic superomniphobic surfaces have been demonstrated,[28,29] major challenges exist in the creation of superomniphobic surfaces with high transparency or optical functionality. Current barriers to realizing superomniphobic optical materials include (i) low optical transmission, (ii) poor optical clarity due to light scattering, (iii) lack of process scalability, (iv) condensation failure, and (v) poor abrasion resistance. Many of the superomniphobic coatings in the literature have no regard for optical transparency.[18,19,30] Additionally, various re-entrant microstructures that have been demonstrated for superomniphobicity[24,27,31] are far too large to provide for anti-reflection. Subwavelength structures such as the 200 to 300 nm sized pillars in moth eyes are needed for antireflection.[32] Poor optical clarity due to high haze is also a major issue. The large difference in refractive index at the solid–air interface of these surfaces results in significant light scattering.[12,33–35] While light scattering is desirable in some optoelectronic applications such as solar cells and LEDs,[36–39] the scattering of light contributes to the blurriness of text and images viewed in displays.[25,40]

Creating superomniphobic surfaces through scalable manufacturing processes is a challenge due to the more demanding requirements for re-entrant micro-/nanostructures that are needed to achieve omniphobicity. Re-entrant structures have generally been achieved by complex micropatterning of a mask followed by some isotropic etch to provide for undercutting.[24,27,29,31] However, the need for patterning limits the scalability of these methodologies. There is much interest in maskless or pattern-free processing methods,[12,33–35] that are generally more scalable to larger areas.

Condensation on glass or so-called fogging can result in poor visibility[7] and destroy the superhydrophobicity of surfaces.[8] Nanostructures with high height over pitch aspect ratios as well as close spacing are desirable for stable Cassie–Baxter wetting.[35,41] However, the need for high aspect ratio structures leads to poor abrasion resistance as tall, thin nanostructures can be easily scratched off. Indeed, many natural surfaces such as insect wings or eyes tend to be very fragile under abrasion.[42]

Identifying a fabrication process for a high performance and multifunctionalized substrate with random nanostructures requires allowing great freedom in the possible fabrication process. Consequently, the number of process parameters for creating these nanostructures is often high-dimensional, with many etching and deposition process parameters that may be varied. Searching this space of possible fabrication strategies is often limited to grid-like search methods where a particular process parameter is systematically varied based on physical intuition. That research approach is only effective to very small localized regions of the input parameter space and only in low dimensional spaces.

In this paper, we address these challenges by combining a Bayesian machine learning procedure with our physical intuition to create a new high performance glass. To create this new glass, we demonstrate a design process that utilizes Bayesian learning and optimization[43–45] to facilitate an efficient search of this multi-dimensional fabrication space. To balance the photon management and wettability properties, we posed a multiobjective optimization problem, where a subset of the Pareto efficient frontier is explored subject to pre-defined threshold values (as stated using expert physical intuition). Gaussian processes are built using existing experimental data, and then updated after each 5 experimental fabrications (which are conducted in parallel batches of 5 to facilitate a faster search). These batches of 5 fabrication strategies were devised to maximize a modified form of expected improvement, which defines the utility of identifying high performing fabrication parameters subject to their viability of satisfying the thresholds.

Using this approach, we demonstrate the successful creation of a new self-healing, durable superomniphobic glass with ultra-high transparency and ultralow haze. Inspired by recent analysis of glasswing butterfly wings,[3] this research focuses on random nanostructures as opposed to highly ordered sub-wavelength structure arrays that may exhibit undesirable optical diffraction patterns. The glass is demonstrated through a simple, scalable two-step maskless reactive ion etching and fluorination process, which we demonstrate on 4 inch diameter glass wafers. Single-side nanostructured glass exhibits 97.0% total transparency while double-side nanostructured glass exhibits 99.5% at 550 nm wavelength and less than 0.1% haze for both at the same wavelength. The glass shows broadband antireflection (<20%) even at high incidence angles of 70°. The specular reflection for single-side nanostructured glass and double-side nanostructured glass are 5.8% and 4.4% at 45° incident angle, respectively, while normal glass shows 8.3% reflection at the same incident angle. In addition, static water and ethylene glycol contact angles of 162.1 ± 2.0° and 155.2 ± 2.2°, respectively, for fused silica glass were demonstrated. The glass exhibits resistance to condensation or antifogging properties. The glass we reported here shows antifogging efficiency[7] more than 90% and demonstrates water departure of droplets smaller than 2 μm. The glass shows self-healing behavior after 500 mechanical abrasion cycles with an abrasive pad and pressure of 1225 N m^{-2}. The abraded glass can recover its high water and oil contact angle after heating for 15 minutes.

Fabrication strategy

The nanofabrication process is performed in two steps: (a) reactive ion etching (RIE) and (b) plasma enhanced chemical

vapor deposition (PECVD) and surface treatment with fluorination. This fabrication process scalably creates the nanostructures directly into the fused silica glass without the need for patterning or an external mask.[33,34] Fig. 1 depicts the input and output parameters under analysis, and suggests how we efficiently optimize this process (which we discuss in greater detail later in this article). Nine input process parameters were considered: (1) the CHF_3 flow rate, (2) the Ar flow rate, (3) the O_2 flow rate, (4) the $CF4_3$ flow rate, (5) the SF_6 flow rate, (6) the etching time, (7) the radio frequency (RF) power, (8) the pressure of the etch chamber, and (9) the SiO_2 deposition time. The first eight parameters are associated with the first processing step, while the last parameter is associated with the second processing step.

The first fabrication step focuses on RIE to create sub-wavelength nanostructures in the fused silica in order to maximize the total transparency and minimize the haze at the wavelength of 550 nm. In the RIE process, the etch chamber is pumped down to high vacuum and then an etching gas is flowed into the chamber. Next, a 13.56 MHz radio-frequency (RF) power is applied to a pair of parallel electrodes which generates a plasma. Reactive species, such as ions and radicals, and monomers are formed when the etch gas is dissociated in this plasma. These reactive species and monomers are transported onto the substrate surface by the electric field and react with the etch target material and competitive reactions of etching and deposition take place near the surface.[46] The morphology of the etched nanostructures depend strongly on the RIE process parameters such as the pressure, gas chemistry, and RF power.

The second processing step focuses on creating re-entrant structures and a low energy surface. In this processing step, we consider the deposition of silicon dioxide (SiO_2) by PECVD on top of the sub-wavelength nanostructures in order to make the structure re-entrant followed by flourination.[35] We focus on varying the deposition time, which affects the amount of SiO_2 deposited, while all the other processing parameters are fixed. Previous research has demonstrated that a concave (re-entrant) surface formed by roughness upon microscale features results in local energy minimization and these surfaces are capable of pinning the liquid–air interface. These structures stabilize the Cassie–Baxter wetting state, which results in high contact angle for different liquids with various surface energy.[22,47] In PECVD, the pressure of the chamber and the power were set at 900 mTorr and 60 Watt, respectively. The flow rate of silane/nitrogen (SiH_4/N_2) and dinitrogen monoxide (N_2O) were both 140 sccm. The thickness of the SiO_2 layer can be controlled by the deposition time. In our process, the deposition rate was approximately 110 nm min^{-1}. The temperature of the PECVD chamber was fixed at 400 °C.

The structures were modified with flourosilane after SiO_2 deposition to create a low surface energy surface by spin coating method. Tridecafluorooctyl triethoxysilane (FAS, Dynasylan F 8261) was mixed with trimethoxy(1*H*,1*H*,2*H*,2*H*-heptadecafluorodecyl)-silane (with ratio of 5 : 1 vol%) and the solution was dispersed in ethanol (5 : 1 vol%).[22] The final solution was spin coated on the glass substrates for 60 s at 1500 rpm, followed by annealing at 95 °C for 10 min. The substrates were then cleaned with acetone and dried with nitrogen.

We focused on optimizing three output parameters: (1) maximize transparency, (2) minimize haze, and (3) maximize oil static contact angle. The optical properties were characterized using a spectrophotometer (PerkinElmer, Lambda 750), equipped with a 60 mm integrating sphere. The angle-resolved reflection spectra was measured on an Agilent UV-Vis-NIR Cary-series spectrophotometer system. A large (6°) detector aperture was used to ensure all light was collected from the narrow source beam (1° apertures) at high incident angle. At each angle the reflection spectra was collected in a narrow band around 550 nm (±5 nm) in 1 nm increments and averaged. This process was performed for both TE- and TM-polarizations. The unpolarized spectra were calculated from the average of the TE and TM polarized light.

The liquid contact angles were measured using an Attension Theta optical tensiometer. For the condensation test, a humidifier and dehumidifier were used to control and set the humidity of the

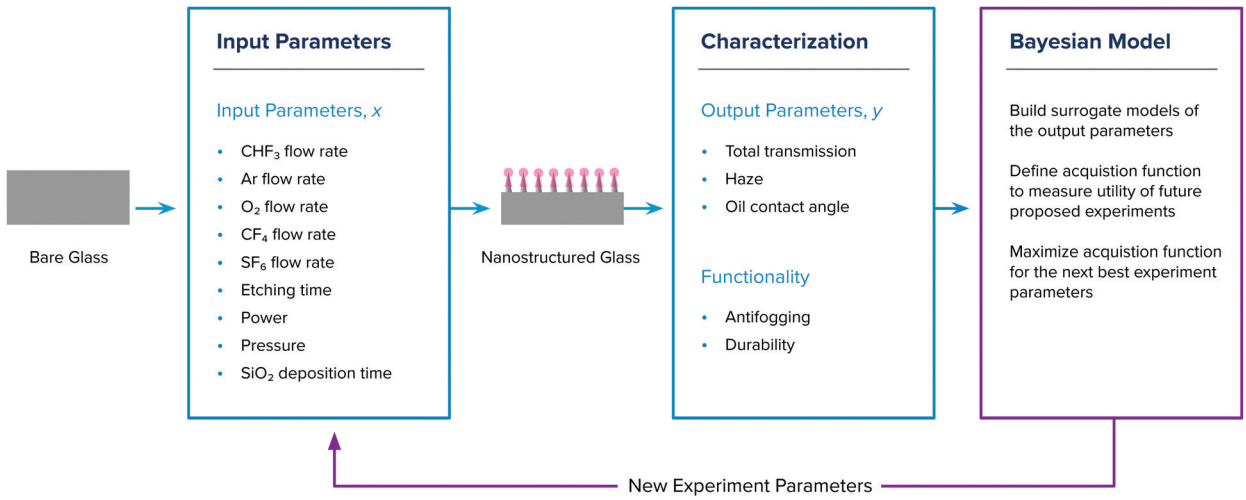

Fig. 1 Schematic of experimental fabrication and Bayesian learning optimization process for nanostructured glass.

system to specific values. Samples were held vertically, while a humidity control was used to set the humidity of the surrounding area to 80%. The Attension Theta optical tensiometer was used to observe the formation of droplets on the substrates. The relative humidity was sustained for 45 minutes while a video was recorded at 1 frame per second.

Experimental design methodology

We consider the fabrication of nanostructured substrates as defined in the previous section, where we simultaneously want high performance photon management and wetting properties (Fig. 1), as a multiobjective optimization problem with solution x^*,

$$x^* \text{ satisfies} \begin{cases} x^* = \arg\max_{x\in\mathcal{X}} & T_{\text{total}}(x), \\ x^* = \arg\min_{x\in\mathcal{X}} & H(x), \text{ and} \\ x^* = \arg\max_{x\in\mathcal{X}} & \theta_{\text{o}}(x) \end{cases} \tag{1}$$

where $\mathcal{X}$ is the space of all possible choices of the process parameters. We denote x to be both the fabrication process parameters and the resulting nanostructure from using those parameters. T_{total} is the total transmission, H is the haze, and $\theta_{\text{o}}(x)$ is the oil contact angle.

The total transmission and haze are optimized for wavelength λ = 550 nm, which is in the middle of the visible spectrum, and ethylene glycol was chosen as the oil. The wavelength-dependent haze $H(\lambda)$ is defined as

$$H(\lambda) = \left[\frac{T_{\text{scattered}}(\lambda)}{T_{\text{total}}(\lambda)}\right] \times 100\%, \tag{2}$$

where $T_{\text{total}}(\lambda)$ is the total transmission and $T_{\text{total}}(\lambda) = T_{\text{scattered}}(\lambda) + T_{\text{specular}}(\lambda)$, where $T_{\text{scattered}}$ is the scattered transmission and T_{specular} is the specular or direct transmission.

In general, there is no unique structure x^* that is simultaneously optimal in all the objectives in eqn (1). In lieu of such a point, the solution to such a multiobjective problem is often defined as the Pareto-optimal set, or Pareto-efficient frontier $\mathcal{P} \in \mathcal{X}$. Pareto optimal parameters $x \in \mathcal{P}$ evince a "balance" between objective function values, such that no $x' \in \mathcal{X}$ can yield better performance across all objective functions; any improvements in one metric would necessitate a loss in performance in at least one other metric (thus the sense of balance). A more thorough explanation of the topic can be found in multicriteria literature.[48]

Standard Bayesian optimization

Bayesian optimization is a sample-efficient iterative search framework, where the relationship between process parameters and objective function values is unknown, and function evaluations (executing the fabrication and characterizing the resulting substrate) are expensive or time consuming. Standard Bayesian optimization consists of two components: a probabilistic surrogate model, to model the objective function f, and an acquisition function, to determine which x parameters to next sample.

In a typical single objective Bayesian optimization setting, the objective function f is assumed to be a realization of a Gaussian process (GP) with mean function μ and a positive definite covariance kernel K, *i.e.*, $f \sim \mathcal{GP}(\mu, K)$.[49,50] After k observed function evaluations have taken place, the resulting data may be denoted as $\mathcal{D}_k = \{(x_1, y_1), \ldots, (x_k, y_k)\}$; we write $|\mathcal{D}_k| \equiv k$ to say that k observations comprise our data. The mean and covariance functions are often defined to have certain free parameters which are fit to the data $\mathcal{D}_k$ using strategies such as maximum likelihood estimation (MLE, which was our strategy of choice in this process). In all of our modeling, we assume our GPs to have $\mu \equiv 0$ and a square-exponential K with independent length-scales in each dimension. A Tikhonov parameter is fixed to be 10^{-3}, primarily to ease ill-conditioning concerns.

An acquisition function is a utility function that measures the value of sampling at different points within $\mathcal{X}$, given what data has already been observed. Acquisition functions balance the trade-off between exploitation, suggesting input parameters near where we have the best results so far, and exploration, suggesting input parameter in regions where we have not tried out. After k different input parameters have been tested, the kth surrogate model can be created, which allows the formation of the acquisition function, which is then maximized to determine the x_{k+1} input parameter selection at which to run the fabrication process.

Modifications to Bayesian optimization

We describe our adaptation of Bayesian optimization to efficiently search for input parameters which address eqn (1). The strategy has some decisions unique to this scenario, but can be generalized to an arbitrary number of objectives.

The first modification to note is that, unlike the traditional sequential nature of Bayesian optimization, we chose to run 5 simultaneous fabrication processes. This allowed us to accelerate the parameter search, which was valuable because the fabrication process can take more than a couple hours. The specifics of this parallel Bayesian optimization[51] are explained later.

The strategy is derived from the ε-constraint method.[52] We transform the multiobjective optimization problem eqn (1) to three constrained scalar optimization problems:

$$\max_{x\in\mathcal{X}} T_{\text{total}}(x), \quad \text{s.t. } H(x) \le \hat{H} \text{ and } \theta_{\text{o}}(x) \ge \hat{\theta}_{\text{o}}, \tag{3a}$$

$$\min_{x\in\mathcal{X}} H(x), \quad \text{s.t. } T_{\text{total}}(x) \ge \hat{T}_{\text{total}} \text{ and } \theta_{\text{o}}(x) \ge \hat{\theta}_{\text{o}}, \tag{3b}$$

$$\max_{x\in\mathcal{X}} \theta_{\text{o}}(x), \quad \text{s.t. } T_{\text{total}}(x) \ge \hat{T}_{\text{total}} \text{ and } H(x) \le \hat{H}, \tag{3c}$$

where $\hat{T}_{\text{total}}$, $\hat{H}$ and $\hat{\theta}_{\text{o}}$ are pre-defined thresholds. These quantities define viability for this experimental setting – we only consider parameter choices x to be viable if all three constraints are satisfied, *i.e.*,

$$T_{\text{total}}(x) \ge \hat{T}_{\text{total}}, \quad H(x) \le \hat{H}, \text{ and } \theta_{\text{o}}(x) \ge \hat{\theta}_{\text{o}} \tag{4}$$

For the parameter search conducted here, $\hat{T}_{\text{total}}$ = 88.5%, $\hat{H}$ = 1.1%, and $\hat{\theta}_{\text{o}} = 60^\circ$.

Another modification to the standard Bayesian optimization methodology accounts for the physical limitations in the precision of executing a proposed fabrication strategy. The parameters defining $\mathcal{X}$ are fundamentally continuous (*e.g.*, the etching time can be any positive real number), but the actual tooling and machinery used in the fabrication process have limited precision and small changes in the input parameters do not result in quantifiable differences in the created structure. As a result, the actual domain under analysis is a discrete domain designed to account for a minimum difference (distance in parameter space) between proposed fabrication strategies. That space is:

- CHF_3 flow rate: {0, 5,. . .,80} sccm,
- Ar flow rate: {0, 5,. . .,100} sccm,
- O_2 flow rate: {0, 5,. . .,100} sccm,
- CF_4 flow rate: {0, 5,. . .,80} sccm,
- SF_6 flow rate: {0, 5,. . .,80} sccm,
- Etching time: {0, 60,. . .,5400} seconds,
- Power: {20, 30,. . .,300} watts,
- Pressure: {50, 100,. . .,250} mTorr,
- SiO_2 deposition time: {8, 10,. . .500} seconds.

The substrate fabrication process described above is time-consuming, which necessitates an effective experimental design so as to quickly search the space $\mathcal{X}$ for input parameters which perform well for all three objective functions. The entire 9-dimensional space consists of over 7×10^{12} experiments. Each single experiment can take 2–3 hours to complete, in addition to requiring the use of various resources, which makes it practically impossible to search through whole space to find the optimum values.

Because the circumstances of eqn (3) are more complicated than a standard Bayesian optimization setting, we require more complicated models and a modified acquisition function. We adapt methods from constrained Bayesian optimization literature.[53] After k fabrications have been conducted, the available data for each of the objectives, denoted $\mathcal{D}_{T,k}$, $\mathcal{D}_{H,k}$ and $\mathcal{D}_{\theta,k}$, allows us to create Gaussian process models $s_{T,k}$, $s_{H,k}$ and $s_{\theta,k}$ for the transmission, haze and contact angles, respectively. These are modeled independently, though in future work we could consider a joint model. For conciseness, we will represent the accumulation of all three data objects with a single symbol, $\mathcal{D}_k$.

Using these models, an acquisition function is defined for each component of eqn (3). This acquisition function is modified from the expected parallel improvement[54] to account for the desire for viability. Considering, at first, only the solution to eqn (3a), imposing the viability requires us to consider not only the distribution of $t \sim s_{T,k}(x)$ (a Gaussian distribution), but the joint distribution t, h, $z \sim s_{T,k}(x)$, $s_{H,k}(x)$, $s_{\theta,k}(x)$, more succinctly denoted by t, h, $z \sim \mathbf{s}_k(x)$. The acquisition function (without parallel suggestions) would be defined as

$$a_{T,k}(x) = \mathbb{E}_{t,h,z \sim \mathbf{s}_k(x)}[(t - \tilde{t}_k)_+ I_{\mathrm{h} < \hat{H} \cap z > \hat{\theta}_\mathrm{o}}], \qquad (5)$$

where $\tilde{t}_k$ is the highest T_{total} value observed thus far, $(\xi)_+$ denotes $\max(\xi,0)$, and $I_\nu = 1$ if the condition ν is satisfied and 0 otherwise (the indicator function). This is semantically equivalent to maximizing the expected improvement attainable for viable points; points which do not satisfy our thresholds contribute zero improvement.

To account for the desire for 5 parallel suggested parameters, we expand on the base structure of eqn (5). We further expand our notation by using $x_{k,\ell}$ to denote the ℓth of 5 points to be simultaneously tested, $x_{k,1}, \ldots, x_{k,5} \in \mathcal{X}$, given the data $\mathcal{D}_k$ which has already been accumulated. Distributions of the t, h, z values at each of these 5 points is denoted with the shorthand notation

$$\mathbf{t}, \mathbf{h}, \mathbf{z} \sim \mathbf{s}_k(\mathbf{x}) \Leftrightarrow t_1, h_1, z_1, \ldots, t_5, h_5, z_5, \sim \mathbf{s}_k\left(x_{k,1}\right), \ldots, \mathbf{s}_k\left(x_{k,5}\right).$$

This allows us to write the expected parallel improvement, attenuated by viability, for transmission with ℓ parallel suggestions as

$$a_{T,k,\ell}\begin{pmatrix} x_{k,1} \\ \vdots \\ x_{k,\ell} \end{pmatrix} = \mathbb{E}_{\mathbf{t},\mathbf{h},\mathbf{z} \sim \mathbf{s}_k(\mathbf{x})}\left[\max_{1 \le i \le \ell} (t_i - \tilde{t}_k)_+ I_{h_i > \hat{H} \cap z_i > \hat{\theta}_\mathrm{o}}\right], \quad (6a)$$

with analogous acquisition functions for the haze,

$$a_{H,k,\ell}\begin{pmatrix} x_{k,1} \\ \vdots \\ x_{k,\ell} \end{pmatrix} = \mathbb{E}_{\mathbf{t},\mathbf{h},\mathbf{z} \sim \mathbf{s}_k(\mathbf{x})}\left[\max_{1 \le i \le \ell} \left(h_i - \tilde{h}_k\right)_+ I_{t_i > \hat{T}_{\mathrm{total}} \cap z_i > \hat{\theta}_\mathrm{o}}\right], \quad (6b)$$

and oil contact angle,

$$a_{\theta,k,\ell}\begin{pmatrix} x_{k,1} \\ \vdots \\ x_{k,\ell} \end{pmatrix} = \mathbb{E}_{\mathbf{t},\mathbf{h},\mathbf{z} \sim \mathbf{s}_k(\mathbf{B})}\left[\max_{1 \le i \le \ell} \left(\theta_i - \tilde{\theta}_k\right)_+ I_{t_i > \hat{T}_{\mathrm{total}} \cap h_i < \hat{H}}\right]. \quad (6c)$$

In lieu of a standard mechanism to merge these acquisition functions, which does not exist in the literature, we executed the following strategy. We identify the next points at which to fabricate, $x_{k,1}$ through $x_{k,5}$, sequentially by randomly choosing one of eqn (6a)–(6c) to optimize for each point. For example, we could randomly choose to optimize for transmission with $x_{k,1}$, which means that we would maximize $a_{T,k,1}$. After that, we could choose to maximize eqn (6c), $a_{\theta,k,2}$, with $x_{k,1}$ fixed to find $x_{k,2}$; this process is repeated up to $x_{k,5}$.

Our full strategy is explained in Algorithm 1. We explicitly state the potential for initial data $\mathcal{D}_{b_i}$ in the algorithm, but no initial data is required. In the experiment we conducted, 79 previous fabrications comprised $\mathcal{D}_{b_i}$.

To prevent fabrication time being spent on suggested parameters x which we believe will perform poorly, we allow ourselves the opportunity to immediately reject parameters. To record such a failed suggestion for a given location x, we append the worst values ever observed for T_{total}, H and θ_o, denoted T_F, H_F and θ_F, to the current data; these values can be updated if worse values are observed in the future. Other strategies, such as maintaining an

explicit model of viability, could be used—this strategy is utilized because it requires no additional modeling hyperparameters.

Algorithm 1 Our Three Objective Bayesian Optimization

input: pre-evaluated data $\mathcal{D}_{b_i}$, experiment budget b
Place a GP prior on f
Initialize $\mathcal{D}_k$ with $\mathcal{D}_{b_i}$, fabrication counter β with 0
while $\beta < b$ **do**
  Fit GP hyperparameters to $\mathcal{D}_k$ with MLE
  for $\ell = 1,\ldots,5$ **do**
    Choose $a_{k,\ell}$ randomly from eqn (6a)–(6c)
    Fit GP models in $\mathbf{s}_k$ to $\mathcal{D}_k$ with MLE
    Optimize $a_{k,\ell}$ with $x_{k,1},\ldots,x_{k,\ell-1}$ fixed to find x'
    if x' is deemed a failed suggestion **then**
      Set $\mathcal{D}_k \leftarrow \mathcal{D}_k \cup (x', T_F, H_F, \theta_F)$
      Repeat Fit and Optimize steps above
    else
      Set $x_{k,\ell} \leftarrow x'$
  Simultaneously fabricate glass with $x_{k,1},\ldots,x_{k,5}$
  Measure T_{total}, H, θ_o for each fabrication
  Set $\mathcal{D}_k \leftarrow \mathcal{D}_k \cup \{(x_{k,1}, T_{total}, H, \theta_o), \ldots, (x_{k,\ell}, T_{total}, H, \theta_o)\}$
  Set $\beta \leftarrow \beta + 5$
return All results in $\mathcal{D}_k$ on the Pareto frontier of eqn (1)

In practice, the acquisition functions are estimated through 4000 Monte Carlo iterations, utilizing our ability to independenty draw from the Gaussian distributions $s_{T,k}(x)$, $s_{H,k}(x)$, $s_{\theta,k}(x)$; the probability of viability only impacts eqn (6a)–(6c) implicitly through the indicator function, and thus no explicit model of viability probability is required. We used the CMA-ES[55] optimization strategy (adapted to the aforementioned discrete parameter domain) to maximize all acquisition functions; the evolutionary population is 25, with 100 full iterations and 10 uniform random restarts.

Fig. 2 depicts the Bayesian optimization process in a sample problem reduced to one dimension for ease of understanding. In the first row, 6 locations have already been sampled of the three objectives. In the second row we demonstrate the Gaussian process models that have been built, and the resulting predictions. In the third row, we show the acquisition functions eqn (6a)–(6c) and the maximum of each; for graphing simplicity we omit the parallel suggestion aspect and plot only $a_{T,6,1}$, $a_{H,6,1}$ and $a_{\theta,6,1}$. We also show the explicit probability of viability estimated through Monte Carlo sampling (which is presented simply for display and is not required to compute the acquisition functions). In the final row, we show the Gaussian process models after being updated with data sampled at the 3 suggested points, which would then be used to generate 3 new points at which to sample.

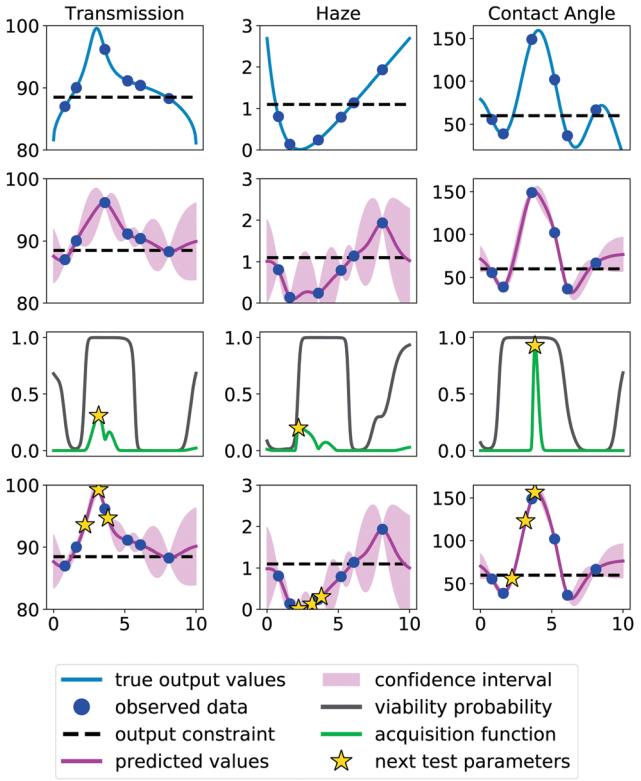

Fig. 2 Sample depiction of our proposed Bayesian optimization process; each column represents one of the three output parameters under consideration. These are artificial profiles in one dimension for explanatory purposes only. First row: The "true" output parameter to be optimized. Second row: Statistical models built from the observed data. Third row: The probability of an input parameter being viable (satisfying the constraints for the other two output parameters) and the associated acquisition function values along with the points which maximize that acquisition function (without any parallel considerations). Fourth row: The new observations achieved by sampling at the "next test parameters" and the new models which result from this new data.

Results and discussion

Fig. 3 plots a summary of the experimental design and Bayesian optimization process. Sixty four experimental runs were conducted in total, of which four were immediately reported as failures as described in Algorithm 1. The left component of Fig. 3 shows the three 2D plots depicting the objective values observed during the Bayesian optimization. In the optimization of the photon management properties (direct transmission *vs.* haze), only a single process condition or structure was determined to be Pareto efficient (the blue star). This indicates that the total transmission and haze are strongly correlated.[36]

As a baseline, smooth glass has 93.5% transmission and 1.5% haze at 550 nm wavelength. After our experimental runs, the transparency increased to 97.0% while the haze value was reduced to 0.1% while improving oil contact angle beyond 150°. In total, five sets of input parameters were identified which are considered viable (satisfy the stated constraints) and Pareto efficient. The trade-off between the objectives is depicted in the rightmost graph of Fig. 3.

Characterizing the nanostructured glass properties

We further characterize the optimally performing nanostructured glass identified from our parameter search. We focus on characterizing the nanostructured glass associated with the blue star

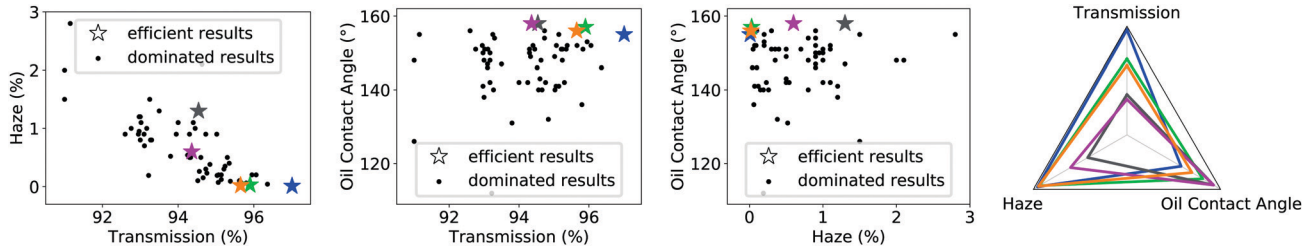

Fig. 3 Depictions of the experimental design driven by our Bayesian optimization methodology. Left: Three 2D feasible region plots of the three objectives under consideration. Right: Radar plot of the 5 viable efficient outcomes identified during the parameter search (plot qualitatively exaggerated to account for the different scales of the three objectives).

in Fig. 3 which has the best optical properties compared with other Pareto efficient datapoints. This specific sample with highest transmission and lowest haze was etched by CHF_3, SF_6, and Ar at 10, 5, and 100 sccm flow rates, respectively. The flow rates for both the CF_4 and O_2 were 0 sccm. The total pressure of the chamber was maintained at 250 mTorr, and the power was set at 120 W. The etch and PECVD times were 2940 and 12 seconds, respectively.

Fig. 4(a) shows a scanning electron microscopy (SEM) images of the sub-wavelength, re-entrant structure. Fig. 4(a)(i) shows 20° tilted SEM image and Fig. 4(a)(ii) and (iii) show cross sectional SEM images with different magnifications. The height of the pillars are approximately 100–500 nm and the distance between the pillars are between 20–100 nm. The diameter of the pillars are between 30–40 nm at the tops and 10–20 nm at the bottoms. The randomness in the height and spacing provide for broadband and omnidirectional antireflection like the glasswing butterfly wings.[3] Furthermore, this randomness also provides for robustness against abrasion as will be discussed later. By depositing the SiO_2, the surface area at the top of the pillars increase which provide the re-entrant structures required for omniphobicity.

To investigate the omniphobic property, we deposited drops of different liquids with different surface tensions, from water (72.8 mN m^{-1}) to ethylene glycol (47.7 mN m^{-1}), on both bare and nanostructured substrates. The volumes of the droplets were 5 μl. Three measurements were made for each sample and the mean and standard deviation for each sample are reported. Fig. 4(b)(i) shows the static contact angle of a variety of liquids

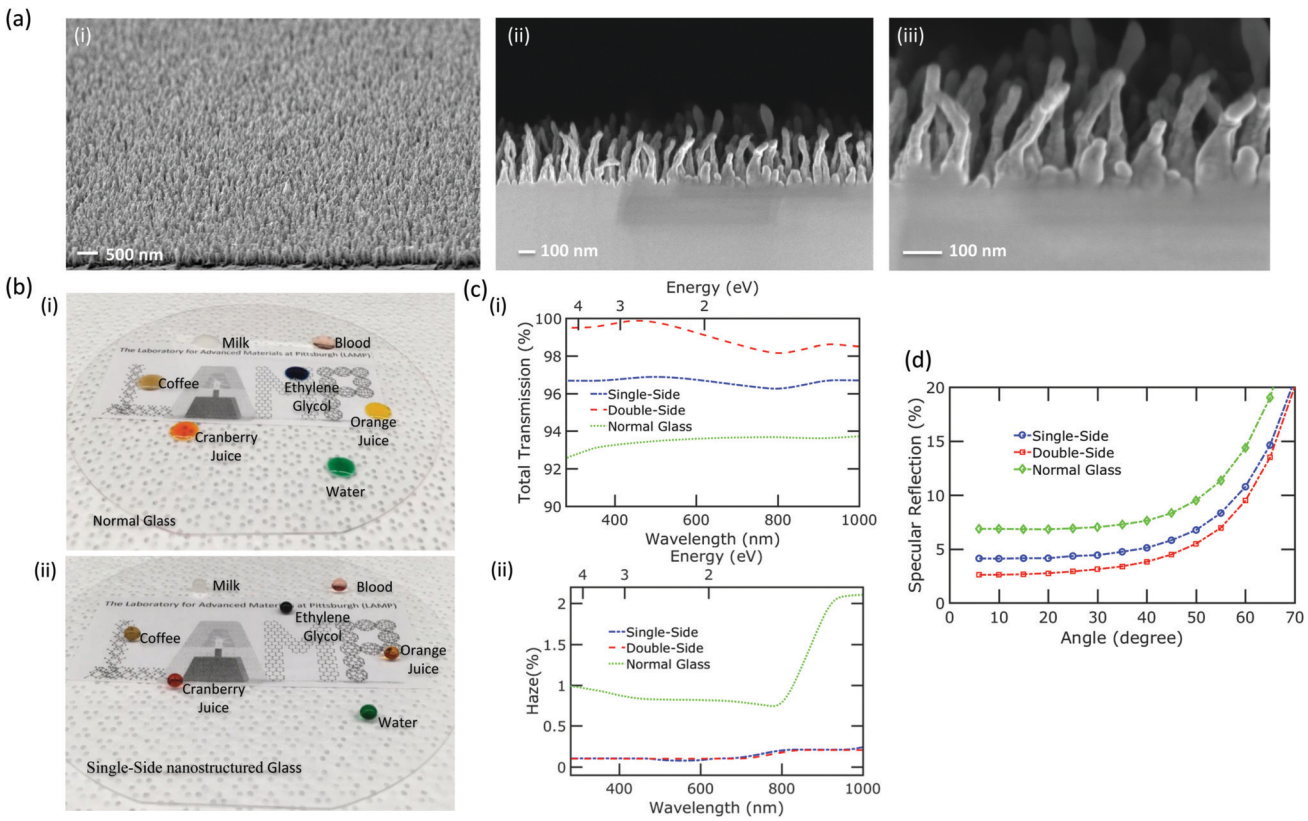

Fig. 4 (a) (i) Shows 20° tilted, (ii) and (iii) cross sectional SEM images of fabricated glass with different magnifications. (b) Droplets of different liquids on (i) normal and (ii) our superomniphobic glass. (c) (i) Transmission and (ii) haze plots as a function of wavelength for bare, single side and double side etched glass. (d) Angle-resolved spectra for reflection at 550 nm wavelength for bare, single side and double side etched glass.

on top of normal glass. The bare fused silica has 42.9 ± 1.1° and 18.7 ± 0.7° contact angle for water and oil, respectively, with 35.5 ± 2.7° hysteresis value for water. The hysteresis value for oil is not measurable, because it is very close to the contact angle. By creating re-entrant structure on the bare fused silica, the water and oil contact angles increase significantly to 162.1 ± 2.0° and 155.2 ± 2.2° with 3.2 ± 0.7° and 9.4 ± 3.6° hysteresis, respectively (Fig. 4(b)(ii)). The contact angle for milk, coffee, blood, cranberry juice, orange juice, and water are all more than 158.0 ± 3.0° with hysteresis less than 8.0 ± 2.0°. Also, as shown in Fig. 4(b)(ii), the transparency of the nanostructured glass is high with no observable reflection and the text beneath the substrate is clearly visible.

Fig. 4(c)(i) and (ii) show the total transmission and haze results for glass as a function of wavelength. As shown in Fig. 4(c)(i), the total transmission for bare fused silica is 93.5% and increases to 97.0% at 550 nm. The transmission spectra for both the bare glass and single-side nanostructured glass are fairly flat across the entire range of 280 to 1000 nm wavelength. The total transmission for the bare glass is between 93.1% to 94.0%, and the total transmission for the nanostructured glass is between 95.9% to 97.1%. The same nanostructures were also created on both sides of the glass and the total transmission of the double-side nanostructured glass at 550 nm is 99.5%. The transmission spectra for the double-sided glass is also fairly flat with total transmission between 98.1% to 99.9%. The corresponding values for haze are shown in Fig. 4(c)(ii). In both single-side and double-side nanostructured glass, the haze value reduces to less than 0.1% across a broadband range of wavelengths. For normal glass the haze value is between 2.2% and 0.9%; however, for nanostructured glass the haze value is fairly flat for the spectrum.

Angle-resolved spectra of specular reflection was recorded at 550 nm wavelength. Fig. 4(d) shows the angle dependent specular reflection for normal glass, single side, and double side nanostructured glass. All the values of reflection for etched glass are less than 5% for both single side and double side etched glass up to 45°. However the reflection values are always less than glass even for a high incidence angle of 70°, which reveals the high omnidirectional, antireflective performance of our fabricated glass.

Characterizing the nanostructured glass functionality

We characterized the water-repellency of the nanostructured glass when exposed to fog. The nucleation of small droplets in the structure may destroy the superhydrophobicity of the surface.[56] However, nanostructured texturing as well as reentrant structures may provide for efficient antifogging by preventing nucleating droplets from growing within the structure and transition to a Wenzel state of wetting.[7,8] To produce condensation, we dispense water at an elevated temperature T_L compared to a constant surface temperature T_S. Water evaporates and condenses on the surface. By increasing the difference between the temperature of the water and surface ($\Delta T = T_L - T_S$, where T_L and T_S are the temperature of liquid and surface, respectively), the amount of condensation increases. Fig. 5(a) shows water jets dispensed with different ΔT on our nanostructured glass (the rate of dispense estimated as 20 ml min^{-1}) (Video S1, ESI†). The results shows that by increasing the ΔT, when the jet reaches the sample, the wetting area increases (Fig. 5(a)(i)) and a number of small water nuclei form (Fig. 5(a)(ii)). However, even with $\Delta T = 70$, the surface retains its super-repellency of water as the droplet can move easily by blowing it off, even without tilting the sample (Video S2 in ESI†). The small water nuclei retain their spherical shape even as they evaporate and easily roll along the surface even at the

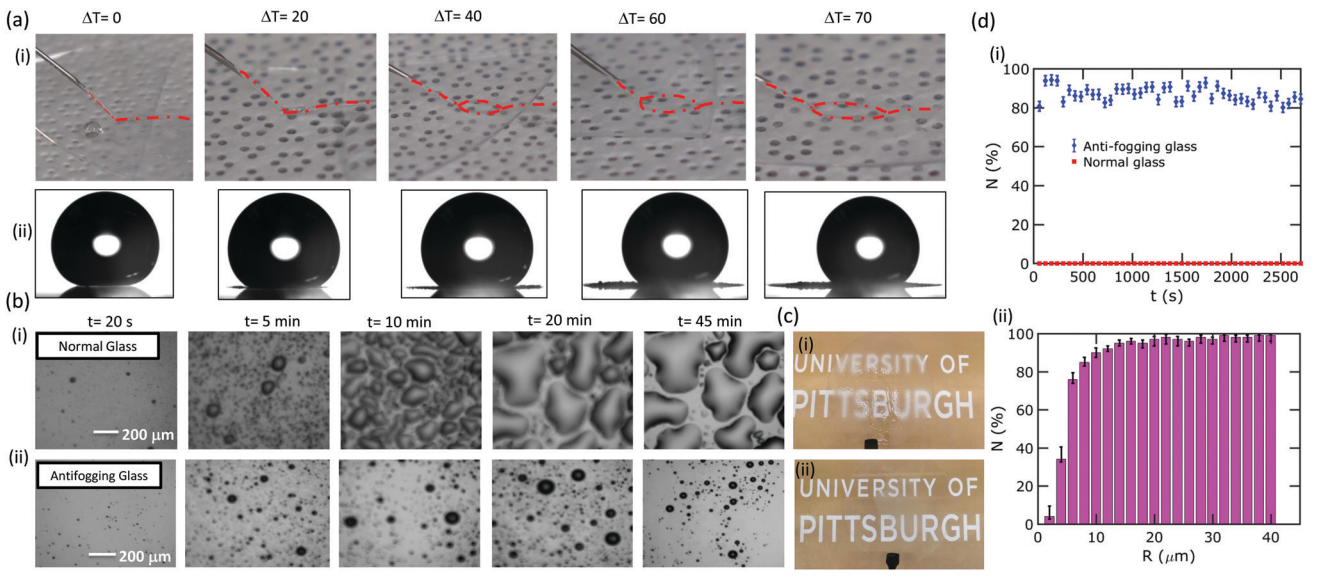

Fig. 5 (a) (i) Water jet behaviour as a function of temperature ΔT. (a) (ii) Water contact angle at different ΔT on antifogging glass. Condensation *versus* time optical images of (b) (i) normal glass and (b) (ii) antifogging glass. (c) Optical image of (i) normal and (ii) antifogging glass after 45 min of condensation. (d) (i) Plot of percentage of droplets dropping after coalescence *versus* time. (c) (ii) Relationship of percentage of coalescences droplets jumping and radius of the droplet at the moment of dropping off.

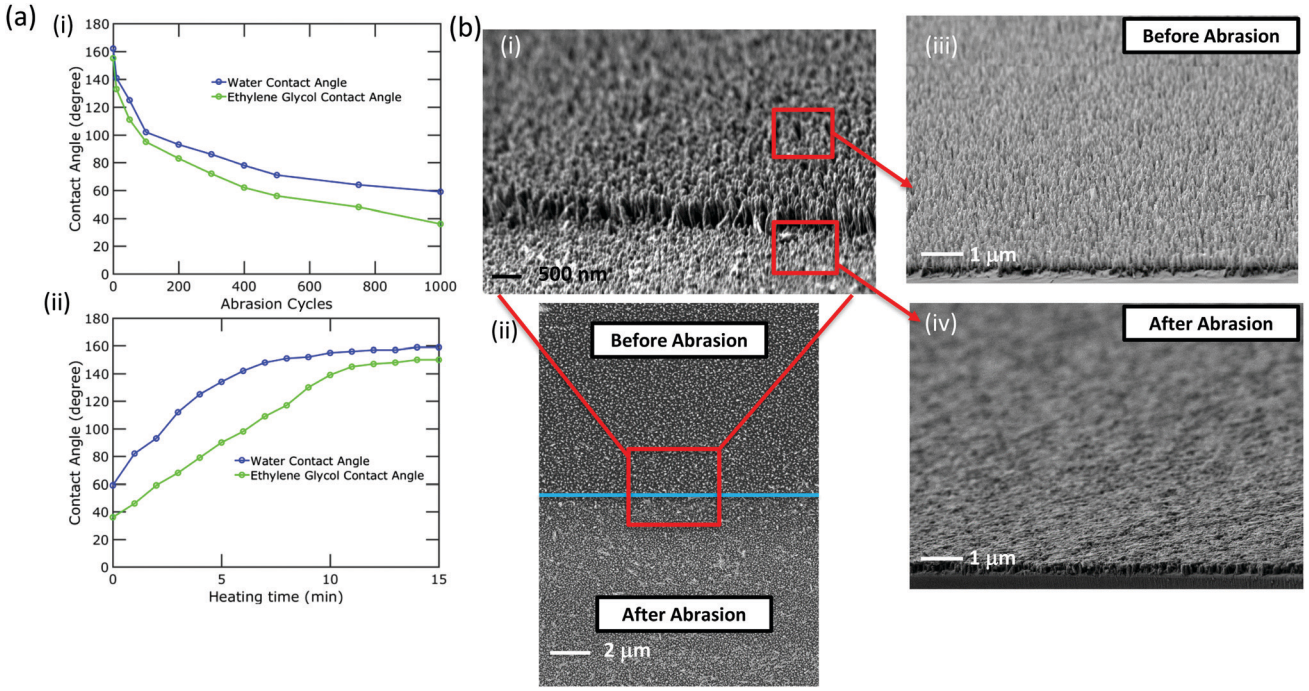

Fig. 6 (a) Water and oil contact angle *versus* (i) abrasion cycle and (ii) after heating the abraded samples. (b) Shows SEM images of (i) 20° tilted and (ii) overhead view of abraded and non-abraded structure with wider view of (iii) non-abraded and (iv) abraded area.

minimum observable diameter of 5 ± 1.0 μm. The corresponding breakthrough pressure associated with this diameter is 30 ± 6.0 kPa.[27]

We also characterized the antifogging properties of nanostructured glass by placing the samples in high relative humidity conditions of 80%. The choice of 80% humidity was based on the high condensation rate in this humid environment. Fig. 5(b)(i) and (ii) show the evolution of fog formation on normal and our nanostructured glass, respectively. In a short time, high density micro-droplets nucleate on both substrates. The difference between normal and antifogging glass, however, becomes apparent after few minutes. While the nucleated droplets grow and coalescence on the normal glass, without falling off of the substrate, the water droplets on the antifogging glass merge together fast and they fall off of the substrate, which provide new nucleation sites for new droplets. This process continues for the whole recorded time (Video S3 in ESI†). The optical images of normal glass and antifogging glass after 45 min condensation are shown in Fig. 5(c)(i) and (ii), respectively.

To quantify the antifogging efficiency, we measured the proportion N of drops falling off the glass after coalescence.[7] After approximately 5000 coalescence events, N *versus* time is plotted in Fig. 5(d)(i) by counting the jumping droplets in one minute. For the normal glass, N is essentially zero for all time because no droplets fall off after coalescence. However, for the nanostructured glass, more than 90% of the coalesced droplets drop off the surface when the size of droplets becomes large enough. The antifogging properties of our nanostructured glass is comparable with the reported values for nanocones with remarkable antifogging abilities.[7] Fig. 5(d)(ii) shows N as a function of droplet radius at the moment of their falling off. The droplets start to jump as soon as their size is as small as 2 μm. The percentage of jumping droplets increase with size of droplet and 99% of droplets above 12 μm jump of the sample. Almost all of the droplets ($N \approx 99\%$) with larger size have jumped out of the substrate.

The mechanical durability of our glass surface comes from two features: its randomness and self-similar structure and ability to self-heal. A Taber Linear Abraser (model 5750) with weighted SCOTCHBRITE abrasive pad was used for abrasion of the samples on a constant surface area of 4×10^{-4} m^2. Fig. 6(a)(i) shows the behavior of water and ethylene glycol contact angle during repeated abrasion cycles with pressure of 1225 N m^{-2}. For both water and oil, the contact angles decrease to less than 90° after approximately 400 cycles of abrasion. However, the mobility of fluorine molecules provides a path for self-healing, similar to that of epitucular wax in plant cuticles.[57] Fig. 6(a)(ii) shows how the water and oil contact angle increase after a heat treatment at 95 °C. After only 15 minutes of heating, the contact angles for both liquids recover. Fig. 6(b)(i) and (ii) show SEM images of tilted and overhead view of the interface between abraded and non-abraded areas of the sample after 500 cycles of abrasion with 1225 N m^{-2} of pressure. The height of the nanostructures decrease, but their reentrant shape is similar to the structure before the abrasion. The randomness of the structures and self-similarity are such that abraded surfaces are similar in texture to the non-abraded surfaces. Fig. 6(b)(iii) and (iv) show the uniformity of the structures over a wide area for non-abraded and abraded samples.

Conclusion

In conclusion, we report superomniophobic, high transmission re-entrant nanostructured glass substrates created using a Bayesian

optimization based experimental design process. The antireflective, superomniphobic glass showed 97.0% and 99.5% total transparency at 550 nm wavelength, for single side and double side nanostructured glass, respectively. In addition, static water and ethylene glycol contact angles of 162.1 ± 2.0° and 155.2 ± 2.2° for fused silica glass have been achieved. The hysteresis for these liquids on glass are 3.2 ± 0.7° and 9.4 ± 3.6°, respectively. Also, the superomniphobic glass can recover its characteristics and heal itself after abrasion through a brief period of heating. The nanostructured glass showed $N \approx 99\%$ antifogging efficiency for broad range of water condensation droplets. In using Bayesian optimization, we explored a complex input parameter space with competing goals to identify and fabricate multifunctional substrates with a very small number of experiments. These substrates can be used in large variety of optoelectronic applications.

Conflicts of interest

There are no conflicts to declare.

Acknowledgements

This work was supported in part by the National Science Foundation (ECCS 1552712).

References

1 F. Xia and L. Jiang, *Adv. Mater.*, 2008, **20**, 2842–2858.
2 D. Stavenga, S. Foletti, G. Palasantzas and K. Arikawa, *Proc. R. Soc. B*, 2006, **273**, 661–667.
3 R. H. Siddique, G. Gomard and H. Hölscher, *Nat. Commun.*, 2015, **6**, 6909.
4 Z. W. Han, Z. Wang, X. M. Feng, B. Li, Z. Z. Mu, J. Q. Zhang, S. C. Niu and L. Q. Ren, *Biosurf. Biotribol.*, 2016, **2**, 137–150.
5 M. I. Kayes, A. Galante, N. A. Stella, S. Haghanifar, R. M. Q. Shanks and P. W. Leu, *Plasma Processes Polym.*, 2018, **128**, 40–46.
6 E. P. Ivanova, J. Hasan, H. K. Webb, V. K. Truong, G. S. Watson, J. A. Watson, V. A. Baulin, S. Pogodin, J. Y. Wang and M. J. Tobin, *et al.*, *Small*, 2012, **8**, 2489–2494.
7 T. Mouterde, G. Lehoucq, S. Xavier, A. Checco, C. T. Black, A. Rahman, T. Midavaine, C. Clanet and D. Quéré, *Nat. Mater.*, 2017, **16**, 658–663.
8 K. L. Wilke, D. J. Preston, Z. Lu and E. N. Wang, *ACS Nano*, 2018, **12**, 11013–11021.
9 X. Zhang, O. Sato, M. Taguchi, Y. Einaga, T. Murakami and A. Fujishima, *Chem. Mater.*, 2005, **17**, 696–700.
10 G. Zhang, D. Wang, Z. Gu and H. Möhwald, *Langmuir*, 2005, **21**, 9143–9148.
11 X. Y. Ling, I. Y. Phang, G. J. Vancso, J. Huskens and D. N. Reinhoudt, *Langmuir*, 2009, **25**, 3260–3263.
12 S. Haghanifar, P. Lu, M. Imrul Kayes, S. Tan, K.-J. Kim, T. Gao, P. Ohodnicki and P. W. Leu, *J. Mater. Chem. C*, 2018, **6**, 9191–9199.
13 D. Nanda, P. Varshney, M. Satapathy, S. S. Mohapatra and A. Kumar, *Colloids Surf., A*, 2017, **529**, 231–238.
14 S. A. Mahadik, M. S. Kavale, S. K. Mukherjee and A. V. Rao, *Appl. Surf. Sci.*, 2010, **257**, 333–339.
15 W. Barthlott and C. Neinhuis, *Planta*, 1997, **202**, 1–8.
16 A. B. D. Cassie and S. Baxter, *Trans. Faraday Soc.*, 1944, **40**, 546.
17 R. N. Wenzel, *Ind. Eng. Chem.*, 1936, **28**, 988–994.
18 S. Pan, A. K. Kota, J. M. Mabry and A. Tuteja, *J. Am. Chem. Soc.*, 2013, **135**, 578–581.
19 W. Choi, A. Tuteja, S. Chhatre, J. M. Mabry, R. E. Cohen and G. H. McKinley, *Adv. Mater.*, 2009, **21**, 2190–2195.
20 A. Ahuja, J. A. Taylor, V. Lifton, A. A. Sidorenko, T. R. Salamon, E. J. Lobaton, P. Kolodner and T. N. Krupenkin, *Langmuir*, 2008, **24**, 9–14.
21 A. K. Kota, Y. Li, J. M. Mabry and A. Tuteja, *Adv. Mater.*, 2012, **24**, 5838–5843.
22 A. Tuteja, W. Choi, M. Ma, J. M. Mabry, S. A. Mazzella, G. C. Rutledge, G. H. McKinley and R. E. Cohen, *Science*, 2007, **318**, 1618–1622.
23 S. Srinivasan, S. S. Chhatre, J. M. Mabry, R. E. Cohen and G. H. McKinley, *Polymer*, 2011, **52**, 3209–3218.
24 X. Liu, H. Gu, M. Wang, X. Du, B. Gao, A. Elbaz, L. Sun, J. Liao, P. Xiao and Z. Gu, *Adv. Mater.*, 2018, **30**, 1800103.
25 B. Sahoo, K. Yoon, J. Seo and T. Lee, *Coatings*, 2018, **8**, 47.
26 Y. Im, Y. Joshi, C. Dietz and S. S. Lee, *Int. J. Micro-Nano Scale Transp.*, 2010, **1**, 79–95.
27 J. Choi, W. Jo, S. Y. Lee, Y. S. Jung, S.-H. Kim and H.-T. Kim, *ACS Nano*, 2017, **11**, 7821–7828.
28 J. Yong, F. Chen, Q. Yang, J. Huo and X. Hou, *Chem. Soc. Rev.*, 2017, **46**, 4168–4217.
29 T. Wu and Y. Suzuki, *Sens. Actuators, B*, 2011, **156**, 401–409.
30 M. Boban, K. Golovin, B. Tobelmann, O. Gupte, J. M. Mabry and A. Tuteja, *ACS Appl. Mater. Interfaces*, 2018, **10**, 11406–11413.
31 S. Min Kang, S. Moon Kim, H. Nam Kim, M. Kyu Kwak, D. Ha Tahk and K. Y. Suh, *Soft Matter*, 2012, **8**, 8563–8568.
32 J. Sun, X. Wang, J. Wu, C. Jiang, J. Shen, M. A. Cooper, X. Zheng, Y. Liu, Z. Yang and D. Wu, *Sci. Rep.*, 2018, **8**, 5438.
33 S. Haghanifar, T. Gao, R. T. R. D. Vecchis, B. Pafchek, T. D. B. Jacobs and P. W. Leu, *Optica*, 2017, **4**, 1522–1525.
34 S. Haghanifar, R. T. R. D. Vecchis, K.-J. Kim, J. Wuenschell, S. P. Sharma, P. Lu, P. Ohodnicki and P. W. Leu, *Nanotechnology*, 2018, **29**, 42LT01.
35 S. Haghanifar, L. M. Tomasovic, A. J. Galante, D. Pekker and P. W. Leu, *J. Mater. Chem. A*, 2019, DOI: 10.1039/C9TA01753D.
36 T. Gao, S. Haghanifar, M. G. Lindsay, P. Lu, M. I. Kayes, B. D. Pafchek, Z. Zhou, P. R. Ohodnicki and P. W. Leu, *Adv. Opt. Mater.*, 2018, **6**(9), 1700829.
37 B. Wang, T. Gao, Z. Zhou, B. Pafchek and P. W. Leu, *J. Photonics Energy*, 2018, **8**, 030501.
38 B. Wang and P. W. Leu, *Nano Energy*, 2015, **13**, 226–232.
39 B. Wang, T. Gao and P. W. Leu, *Nano Energy*, 2016, **19**, 471–475.
40 K. Golovin, D. H. Lee, J. M. Mabry and A. Tuteja, *Angew. Chem., Int. Ed.*, 2013, **52**, 13007–13011.
41 K.-C. Park, H. J. Choi, C.-H. Chang, R. E. Cohen, G. H. McKinley and G. Barbastathis, *ACS Nano*, 2012, **6**, 3789–3799.
42 Y. Si, Z. Dong and L. Jiang, *ACS Cent. Sci.*, 2018, **4**, 1102–1112.

43 B. Shahriari, K. Swersky, Z. Wang, R. P. Adams and N. de Freitas, *Proc. IEEE*, 2016, **104**, 148–175.
44 P. I. Frazier, *Recent Advances in Optimization and Modeling of Contemporary Problems*, INFORMS, 2018, pp. 255–278.
45 D. Packwood, *Bayesian Optimization for Materials Science*, Springer, 2017, vol. 3.
46 K. Nojiri, *Dry Etching Technology for Semiconductors*, Springer, 2012.
47 A. Tuteja, W. Choi, J. M. Mabry, G. H. McKinley and R. E. Cohen, *Proc. Natl. Acad. Sci. U. S. A.*, 2008, **105**, 18200–18205.
48 M. Ehrgott, *Multicriteria optimization*, Springer Science & Business Media, 2005, vol. 491.
49 C. E. Rasmussen and C. K. I. Williams, *Gaussian Processes for Machine Learning (Adaptive Computation and Machine Learning)*, The MIT Press, 2005.
50 G. E. Fasshauer and M. J. McCourt, *Kernel-based Approximation Methods Using Matlab*, World Scientific, 2015.
51 J. Wu and P. Frazier, *Advances in Neural Information Processing Systems*, 2016, pp. 3126–3134.
52 C. Hwang and A. Masud, *Multiple objective decision making, methods and applications: a state-of-the-art survey*, Springer-Verlag, 1979.
53 M. A. Gelbart, PhD thesis, Harvard University, 2015.
54 D. Ginsbourger, R. Le Riche and L. Carraro, A Multi-points Criterion for Deterministic Parallel Global Optimization based on Gaussian Processes, Ecole nationale supérieure des mines technical report, 2008.
55 N. Hansen, S. D. Müller and P. Koumoutsakos, *Evol. Comput.*, 2003, **11**, 1–18.
56 F. Wan, D.-Q. Yang and E. Sacher, *J. Mater. Chem. A*, 2015, **3**, 16953–16960.
57 C. Neinhuis, K. Koch and W. Barthlott, *Planta*, 2001, **213**, 427–434.